ELSEVIER

Spanwise vorticity structure in turbulent boundary layers

J. C. Klewicki
Department of Mechanical Engineering, University of Utah, Salt Lake City, UT, USA

R. E. Falco
SET Enterprises Inc., Fountain Hills, AZ, USA

Four-element hot-wire probe measurements are used to examine the structure of the spanwise vorticity in the inner region of low Reynolds number zero pressure gradient turbulent boundary layers. Single-probe measurements were made over the range $1010 \leq R_\theta \leq 4850 (R_\theta = \theta U_\infty/\nu$, where θ is the momentum deficit thickness, and U_∞ is the free-stream velocity), while two probe measurements were made at $R_\theta \approx 1010$. The present results indicate that for $y^+ < 50$ statistical moment profiles of ω_z scale on inner variables. Event duration analyses indicate that a nearly logarithmic increase in inner normalized time scales of the ω_z bearing motions occurs with increasing R_θ. Outside the buffer region, this R_θ dependence is effectively removed if the Taylor time scale is used to normalize the event durations. Two-point correlations with probe separations in the spanwise as well as wall-normal direction are presented. In addition, the structure of the associated two-dimensional (2-D) probability distributions are examined to reveal the statistically most significant contributions underlying these correlations. Wall-normal probe separation measurements indicate the increasing prevalence of adjacent regions of opposing sign ω_z as the wall is approached. Spanwise probe separation experiments indicate the predominance of single-sign contributions, as well as increasing spatial coherence nearer the wall. The present results are interpreted to indicate that the organized spanwise vorticity-bearing motions are distributed in planes parallel to the wall for y^+ less than about 12, and decrease to a nearly fixed scale outside the buffer region.

Keywords: boundary-layer turbulence; vorticity; coherent motions

Introduction

An ever-growing body of evidence indicates that flow-field interactions associated with coherent vortical motions underly the bulk of momentum and scalar transport in turbulent boundary layers (Robinson 1991; Bernard et al. 1993). The details pertaining to these interactions as well as their dependence on Reynolds number, however, in large part remain poorly understood (e.g., Gad-el-Hak and Bandyopadhyay 1994). The belief by many that vorticity represents the *natural* variable for exploring coherent motion dynamics has prompted an increased emphasis over the past decade in quantifying (either through physical or computational experiments) the time-resolved structure of the boundary-layer vorticity field (see, for example, Wallace and Foss 1995). A major obstacle hindering this effort, however, pertains to the difficulties associated with spatially resolving vorticity fluctuations — especially as the Reynolds number is increased. In physical experiments, this problem generally relates to constructing viable measurement probes with size comparable to the smallest scale of motion within the flow (i.e., on the order of a few viscous units, ν/u_τ). Similarly, computational limitations largely pertain to the computer hardware resources required to generate a simulated flow that faithfully mimics the spatial and temporal evolution of the intended physical flow field.

A number of studies have now reported measurements of the statistical profiles of ω_z (see data in Foss and Wallace 1989; Wallace and Foss 1995). None, however, has explored R_θ dependencies over a significant range for $R_\theta > 1000$. This fact has particular importance regarding interactions between the inner and outer region motions in the boundary layer, because the wake region structure is observed to undergo substantial changes for R_θ less than about 3000 (Antonia et al. 1982; Murlis et al. 1982). In addition, very little physical experiment data exist regarding two- and/or multiple-point vorticity component structure. Kastrinakis (1976) has, however, performed two-point streamwise vorticity correlation experiments in a turbulent channel flow using a four-wire Kovasznay-type probe. (Note that although it was later shown that this probe's response characteristics yielded significant errors in the instantaneous ω_x, Foss and Wallace conclude that the effect of these instantaneous errors "may statistically be small.") Kastrinakis' near-wall measurements yielded peak negative correlations at Δz^+ separations of about 40. In the context

Address reprint requests to Prof. J. C. Klewicki, Dept. of Mechanical Engineering, University of Utah MEB 3209 Salt Lake City, UT 84112, USA.

Received 28 June 1995; accepted 8 February 1996

Int. J. Heat and Fluid Flow 17: 363–376, 1996

655 Avenue of the Americas, New York, NY 10010

0142-727X/96/$15.00
PII S0142-727X(95)00014-7

of coherent motion dynamics, these results represented, perhaps, the first direct evidence of counter-rotating ω_x motions above the wall. Interestingly, however, the presence of a negative correlation disappears for y^+ greater than about 30. Regarding ω_z, the recent study by Rajagopalan and Antonia (1993) presents correlations between the sublayer u fluctuations and buffer region ω_z. In this study, they used a four-wire probe of a type similar to that developed by Foss and Haw (1990). As previously shown by Falco et al. (1990) (as well as herein), their results indicated a strong negative correlation between sublayer and buffer region ω_z.

In contrast to physical experiments, direct numerical simulation (DNS) studies of wall-bounded flows automatically contain the information needed to construct spatial correlations involving vorticity. Studies of this type include the boundary-layer computations of Spalart (1988) ($300 \leq R_\theta \leq 1410$) and the channel flow simulations of Kim et al. (1987) ($R_\theta \approx 300$), and Antonia and Kim (1994) ($280 \leq R_\theta \leq 660$). Interestingly, however, relatively little computationally derived correlation data have been reported. Notable exceptions are the correlation coefficients of ω_z for Δy^+ spacing,

$$\rho_{\omega_z\omega_z}(\Delta Y^+) \equiv \frac{\langle \omega_z(y^+)\omega_z(y^+ + \Delta y^+)\rangle}{\omega_z'^2(y^+)\omega_z'^2(y^+ + \Delta y^+)}$$

for fixed probe at $y^+ = 4.75$ by Kim (reported in Rajagopalan and Antonia 1993), and the $\rho_{\omega_x\omega_x}(\Delta y^+)$, $\rho_{\omega_y\omega_y}(\Delta y^+)$ and $\rho_{\omega_z\omega_z}(\Delta y^+)$ correlations for fixed probe at $y^+ = 15$ reported by Antonia and Kim (1994).

In the present study, the characteristics of ω_z statistical profiles are explored through physical experiments over the range $1010 \leq R_\theta \leq 4850$. Furthermore, a number of inner region two-point correlations of ω_z at $R_\theta \approx 1010$ are also presented. Two-dimensional (2-D) probability density functions (pdfs) are then used to explore the individual ω_z contributions underlying the structure of these correlations.

Experimental conditions and procedures

The experiments were conducted in the 17-meter low-speed wind tunnel previously located in the Turbulence Structure Laboratory at Michigan State University. The test section of this tunnel is 17.1-m long, 1.21-m wide, and nominally 0.61-m high. (The top wall diverged at 0.25° to account for displacement thickness growth.) The zero pressure gradient boundary layers studied developed along the lower wall of the tunnel, and the measurement site was 15.25-m downstream of the tunnel inlet. The boundary layer was tripped approximately 0.5-m downstream of the inlet using a 6.35-mm threaded rod, and the tunnel was operated in its closed return mode in which the laboratory (which has dimensions of 18.3m × 30.5m × 6.1m) is the return plenum.

The experimental results presented herein are derived from the database of Klewicki (1989), where a detailed account of the experimental procedures and information pertaining to the accuracy of the measurements may be found. Much of the same information may also be found in Klewicki and Falco (1990). The single-point measurements were made at three Reynolds numbers $R_\theta = 1010$, 2870, and 4850, while the two-point correlation data were acquired at $R_\theta \approx 1010$. A summary of the principal features of these flows is given in Table 1. Data were obtained with four-wire spanwise vorticity probes similar to that developed by Foss et al. (1986). These probes are comprised of a parallel-array and an x-array arranged as shown in Figure 1. The copper-plated 5-μm diameter tungsten hot-wires contained within the probe are 3-mm in length with a 1-mm center active region. The spacing between the parallel-array wires, Δy, pertinent to the measurement of $\partial u/\partial y$, is nominally 1 mm, as is the spacing of the wires in the x-array. The spacing between the center of the parallel and x-arrays, Δz, is nominally 3.4 mm. For reference, 1 mm is about equal to 1.85, 4.75, and 7.75 viscous units at $R_\theta = 1010$, 2870, and 4850, respectively. Because of the variations in the dissipation rate with y^+, the Kolmogoroff length η $[\equiv (\varepsilon/\nu^3)^{1/4}]$ also varies with y^+. One millimeter ranges between 0.6η and 1.5η at $R_\theta = 1010$, 0.9η to 3.4η at $R_\theta = 2870$, and 1.1η to 4.6η at $R_\theta = 4850$. Regarding the overall resolution of the probe, it is important to note that no gradient contributions to ω_z are computed over the 3.4-mm spacing between the parallel- and x-arrays. There are errors, however, associated with the measurement of $\partial u/\partial y$ and $\partial v/\partial x$ not being co-located. Under the worst case ($R_\theta = 4850$), experiments reported in Klewicki and Falco (1990) indicate that the average instantaneous error in $\partial v/\partial x$ caused by this effect is about 25% at $y^+ \approx 140$. The influence on long-time statistics is, however, much

Notation

DNS	direct numerical simulation
f_c	low-pass cut-off frequency
f_s	sampling frequency
H	boundary-layer shape factor(s)
pdf	probability density function
R_θ	momentum deficit thickness Reynolds number, $U_\infty\theta/\nu$
R_Γ	vortex Reynolds number, Γ/ν
u, v, w	streamwise, wall-normal, and spanwise velocity component fluctuations
U	mean streamwise velocity component
U_∞	free-stream velocity
u_τ	friction velocity, $(\tau_w/\rho)^{1/2}$
x, y, z	streamwise, wall normal, and spanwise Cartesian coordinates

Greek

Γ	circulation
δ, δ_{99}	boundary-layer thickness
ε	dissipation rate
η	Kolmogoroff length
θ	momentum deficit thickness
λ_t	Taylor time scale
ν	kinematic viscosity
ρ	correlation coefficient, mass density
τ_w	mean wall shear stress
ω_x, ω_y, ω_z	streamwise, wall-normal, and spanwise vorticity component fluctuations

Subscripts / superscripts

$\langle\rangle$	denotes time-averaged quantity
$'$	denotes rms value of a fluctuating quantity
$+$	denotes normalization by ν and u_τ
$\sim$	denotes instantaneous quantity (e.g., $\tilde{u} = U + u$)

Table 1
Principal characteristics of the zero pressure gradient boundary layers of the present study

R_θ	U_∞, m/s	δ_{99}, mm	θ, mm	H	u_τ, m/s	f_c, Hz	f_s, Hz
1010	0.607	206	24.8	1.45	0.0282	250	500
2870	1.752	205	24.5	1.40	0.0707	500	1000
4850	2.981	199	24.3	1.38	0.1125	1000	2000

smaller. Near the wall this effect is diminished, because $\partial u/\partial y$ contributions to ω_z dominate those of $\partial v/\partial x$ (see Figure 8).

In the single-probe experiments, DISA model 55M01 anemometers were used at a heating ratio of 1.7. In the two-probe experiments, the second probe was operated using TSI 1755 anemometers. All calibrations were performed in the freestream of the tunnel and employed mean flow data. The x-array calibrations employed an effective angle technique (see Browne et al. 1989 for a comparison of this technique with others). To reduce the possibility of correlated errors in the measurement of $\partial u/\partial y$, the parallel-array elements were calibrated using one of the wires as a reference. A measure of the effectiveness of this procedure is shown in Figure 2, which displays the mean gradient as quantified by the mean difference between the instantaneous velocities from the parallel-array wires at each R_θ. For comparison, the mean gradient computed using the formula of Van Driest (1956) is also shown. An analysis by Klewicki (1989) shows that the small but consistent deviation of the $R_\theta = 1010$ profile from the Van Driest profile results from an additive bias not related to probe body effects, as studied by Böttcher and Eckelmann (1985). Near the wall at $R_\theta = 1010$ the flow speeds were slightly lower than the lower speed limit of the calibration. Numerous comparisons with existing data indicate, however, that under this small extrapolation, the calibrations remained valid. The low flow speeds also caused concern regarding possible natural convection effects. The estimates of Klewicki and Falco (1990) indicate, however, that these effects produce buoyant velocities that are, at worst, less than 3.7% of U. Calibrations were performed immediately before and after each experiment. For the single-probe experiments, the same four wires remained on the probe during the course of acquiring the three different R_θ profiles. This fact is significant in that small measurement differences associated with using a physically different set of wires do not affect the present data comparisons at different R_θ.

The components of $\omega_z (\equiv \partial v/\partial x - \partial u/\partial y)$ were computed using a two-point central difference of the parallel-array data and by differentiating a local (in time) five-point quadratic curve fit of the x-array data. The derivative of the curve fit was chosen over multiple-point finite differencing schemes because it was found to be less susceptible to the effects of system noise, as well as the errors associated with increasing sampling frequency. Taylor's hypothesis was used to convert the time derivative of the x-array data to the streamwise gradient. A moving 100-point average velocity was used as the convection velocity in this procedure. Comparisons of $\partial v/\partial x$ statistics ($y^+ = 12.0$, $R_\theta = 1010$) computed using 50-, 200-, and 500-point average velocities and the mean velocity U indicated that $\partial v/\partial x$ statistics are not sensitive to the choice of convection velocity. For the test case examined, changing the convection velocity resulted in changing the rms spanwise vorticity, ω'_z by a maximum of less than 0.4%. The nondimensional averaging times of the data records were in the range, $3600 \leq TU_\infty/\delta \leq 8600$. The uncertainty associated with the lack of statistical convergence has been determined to be less than 3% for all of the statistical moments presented (Klewicki and Falco 1990). Because the friction velocity is squared when inner normalizing vorticity, uncertainty in the measurement of u_τ can significantly affect profile magnitudes (see Ong 1991; Wallace and Foss 1995). For the purposes of deducing possible R_θ dependencies in the profiles of $\nu\omega'_z/u_\tau^2$, it is, therefore, important that a consistent method for determining u_τ be used. At each Reynolds number of the present study, Clauser plots (based upon the constants of Coles and Hirst 1968) were employed to determine u_τ.

Some conditions were different in the two-probe experiments relative to the single-probe experiments. These are now discussed. Prior to digitization, electronic noise was reduced in the anemometer signals by low-pass filtering at a cut-off frequency of 1000 Hz, which differs from the value of 250 Hz for the

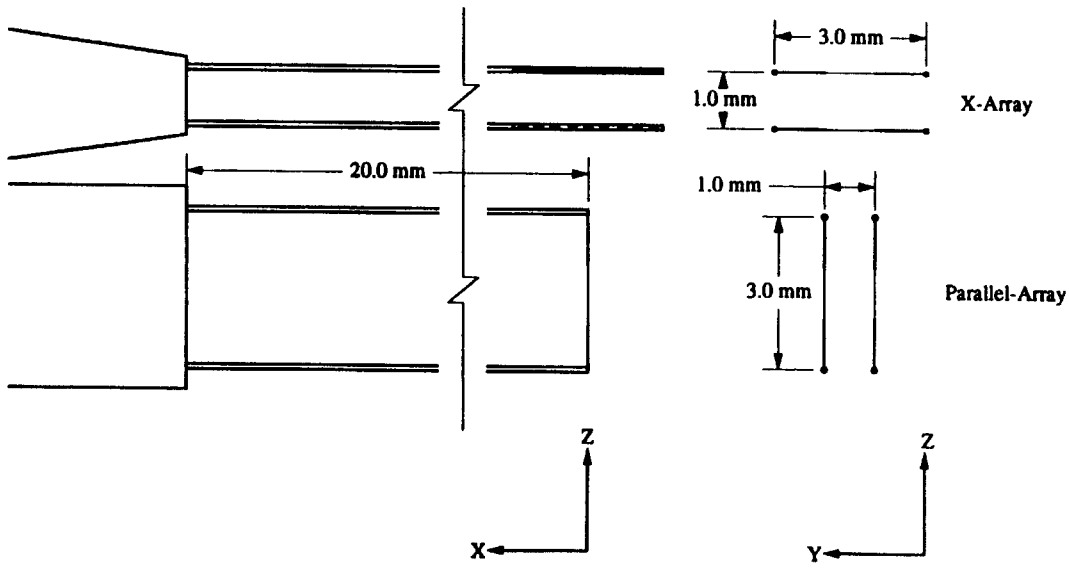

Figure 1 Four element spanwise vorticity probe

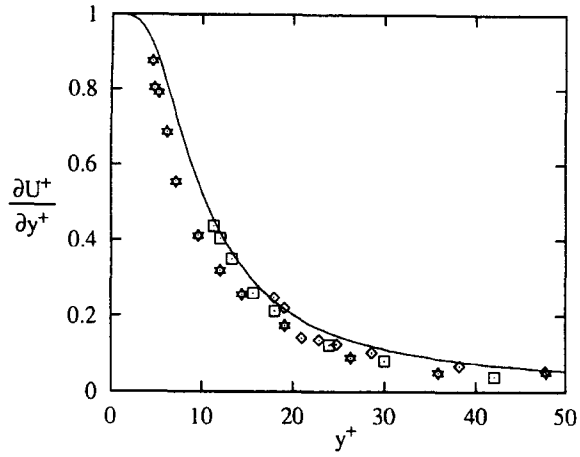

Figure 2 Inner normalized mean velocity gradient derived from the mean of the instantaneous $\partial\bar{u}/\partial y$; $R_\theta = 1010$, ✿; $R_\theta = 2870$, ⊡; $R_\theta = 4850$, ◇ (Van Driest 1956, —)

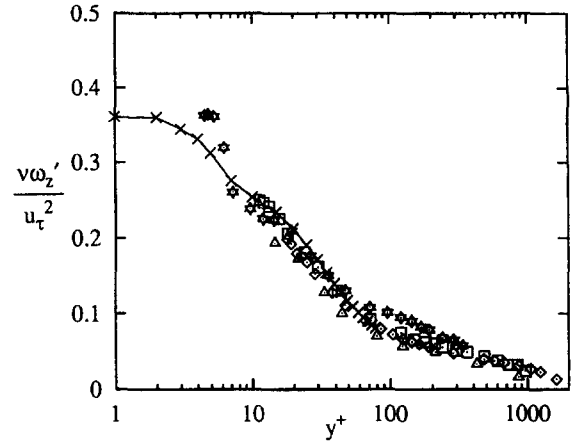

Figure 4 Inner variable normalized spanwise vorticity intensity profiles; data symbols same as in Figure 2 (Balint et al. 1987, $R_\theta = 2100$, △; Kim et al. 1987, $R_\theta = 280$, ✳)

single-probe experiments. Because a second set of filters was required, and this second set had a minimum cut-off capability of 1000 Hz, all signals were analog filtered at 1000 Hz. The data from each of the eight channels (comprising the two four-element probes) were sampled at 250 Hz. Based upon estimates of the dissipation rate ε, as derived from the single-probe measurements, this sampling frequency was about twice the value of the maximum Kolmogoroff frequency, $f_K = U/2\pi\eta$ found in the boundary layer. For each datapoint, the sampling duration was about 6700 integral time scales δ/U_∞. The channel-to-channel phase shift between the different signals was estimated to be less than ± 5 μs. The positions of the probes from the floor as well as the relative positions of the probes in the wall-normal direction Δy^+ were determined using a short-range telescope with cross-hair sight. This method yielded probe center positions (defined as the point at which the wires cross in the x-array) to within ± 0.02 viscous units. Relative probe positions in the z-direction could not be determined as accurately. This reduced accuracy resulted from the initial probe separation being only visually referenced using a 0.254-mm/div. scale and because the z-direction probe center was somewhat arbitrarily chosen to be the internal prong of the parallel-array. The uncertainty in the relative spanwise probe position is estimated to be at most $\pm 1 z^+$.

Single-probe profiles

Statistical structure of the present flow fields has been quantified in a number of previous studies. Mean velocity profiles, as well as profiles of the u and v fluctuations up to fourth moment are reported in Klewicki (1989), and Klewicki et al. (1992). In addition, $\langle uv \rangle$ profiles, velocity–vorticity correlations, and terms in the transport equation for $\langle u^2 \rangle$ are reported in Klewicki et al. (1994). These results show good agreement with previous high-resolution boundary-layer studies, and, in general, confirm that the present flow constitutes a canonical flat plate turbulent boundary layer. In the data presented below, the focus is entirely on the structure of spanwise vorticity and its velocity gradient contributions.

Statistical profiles

Figures 3, 4, and 5 present outer, inner, and mixed variable normalizations of ω_z'. Under the outer variable normalization of Figure 3, a small but discernible Reynolds number trend is observed in the outer part of the boundary layer. This trend becomes increasingly distinct as the wall is approached, and is opposite that which would be indicative of probe resolution-in-

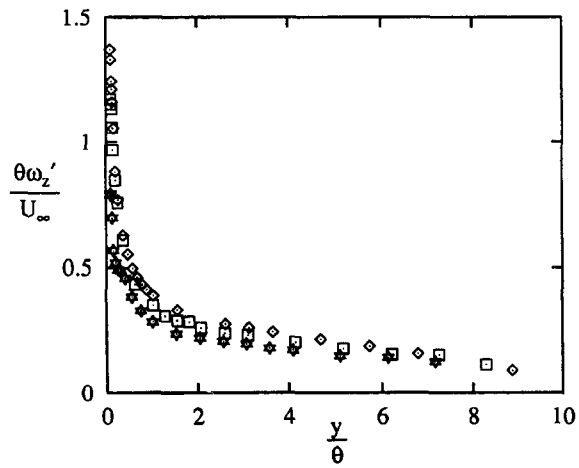

Figure 3 Outer variable normalized spanwise vorticity intensity profiles; data symbols same as in Figure 2

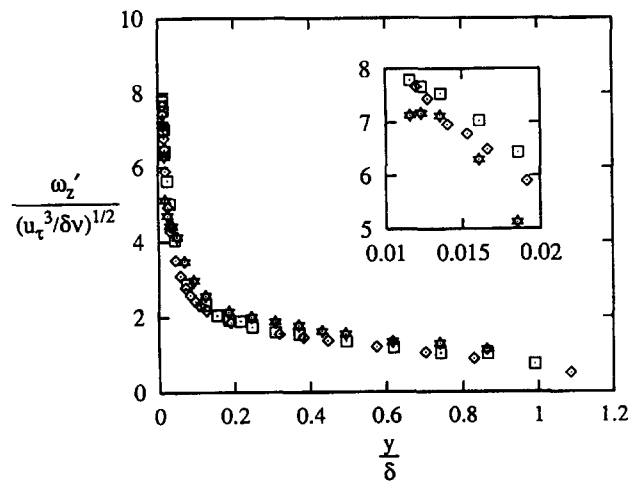

Figure 5 Mixed variable normalized spanwise vorticity intensity profiles; data symbols same as in Figure 2

duced attenuation effects. Thus, measurements with a probe of poorer resolution (with increasing R_θ) might give apparent evidence for invariance under this normalization. Also it is worth noting that normalizing with u_τ and θ (rather than U_∞ and θ) only makes the trend more pronounced, because u_τ/U_∞ decreases with increasing Reynolds number.

The inner normalization of Figure 4 suggests that the three profiles define a single curve for $12 \leq y^+ \leq 80$. This conclusion is reinforced by the fact that at any given y^+ position the value of ω'_z increases by a factor of greater than 10 between the $R_\theta = 1010$ and 4850 profiles. In the inner region, the slight attenuation in the profiles with increasing R_θ has been shown by Klewicki and Falco (1990) to be consistent with spatial resolution effects relating to the measurement of $\partial u/\partial y$. For y^+ greater than about 15, the present data and the results of Kim et al. (1987) are in excellent agreement. It is interesting to note, however, that as the wall is approached, the present $R_\theta = 1010$ profile exhibits a shape different from that of the computational profile — although the two data sets apparently have the same limiting value. Further measurements are required, however, to determine whether this deviation represents more that experimental uncertainty. The present data appear to level off at a value of about 0.37 near the edge of the sublayer. This value is in accord with the findings of Alfredsson et al. (1988) of 0.38 ± 0.02 ($300 \leq R_\theta \leq 2800$) for $\nu\omega'_z/u_\tau^2|_{y=0}$ (see their Table III). Conversely, the merging of the data of Figure 4 for $12 \leq y^+ \leq 80$ does not exhibit the R_θ trend found by Spalart (1988). In his study ($300 \leq R_\theta \leq 1410$) Spalart found that in the wall region the inner normalized ω_z intensity profile displays about a 10% increase over the R_θ range explored. This increase is exemplified by noting Spalart's $\nu\omega'_z/u_\tau^2|_{y=0}$ values, which are 0.38, 0.40, and 0.42 at $R_\theta = 300$, 670, and 1410, respectively. The channel flow study of Antonia and Kim (1994) also indicates an 11% increase in the wall value of $\nu\omega'_z/u_\tau^2$ when R_θ is increased from 280 to 660. For y^+ greater than about 10, however, the different R_θ profiles of Antonia and Kim merge.

Interestingly, Spalart (1988) also indicates that the vorticity intensities define a single curve when plotted versus y/δ and normalized by the mixed scale $(u_\tau^3/\delta\nu)^{1/2}$. Figure 5 shows the present data under this normalization. Over most of the boundary layer, the three distributions exhibit very good agreement. The trend of the data shown in the insert to the figure illustrates, however, that for $y/\delta < 0.02$ the profiles will diverge. Such a conclusion can be made with confidence, although the deviations between the different R_θ data in this insert are small. This is realized by noting first that the $R_\theta = 1010$ distribution of Figure 4 levels off at a peak value near $y^+ = 4.5$. Thus, the data nearest the wall in Figure 5 are also at their peak — a value of about 7.1. On the other hand, at the same y/δ position, the $R_\theta = 2870$ and 4850 distributions are almost equal to 8. It is known, however, that as y/δ approaches zero, the $R_\theta = 2870$ and 4850 profiles of Figure 5 are going to continue to increase significantly. The expectation (substantiated by the data of Figure 4 and the aforementioned results of Alfredsson et al. 1988) is that these profiles will attain a limiting value near 0.4. Assuming that the $R_\theta = 4850$ $\nu\omega'_z/u_\tau^2$ profile reaches a value of 0.37 at $y^+ = 4.5$, under the normalization of Figure 5 this value would be about 16, or more than twice the peak value in the $R_\theta = 1010$ profile.

For y^+ values greater than about 80, the $R_\theta = 2870$ and 4850 data of Figure 4 and the data of Balint et al. (1987) ($R_\theta = 2100$) show very good agreement. The $R_\theta = 1010$ profile, however, shows discernibly higher values. This deviation is apparently consistent with the structural changes known to occur in the wake region at low R_θ. This deviation also agrees with the hypothesis of Huffman and Bradshaw (1972) relating to the increased dynamical significance of the viscous superlayer at low R_θ — resulting from the direct influence of viscous effects in the outer region. According to the hypothesis of Huffman and Bradshaw,

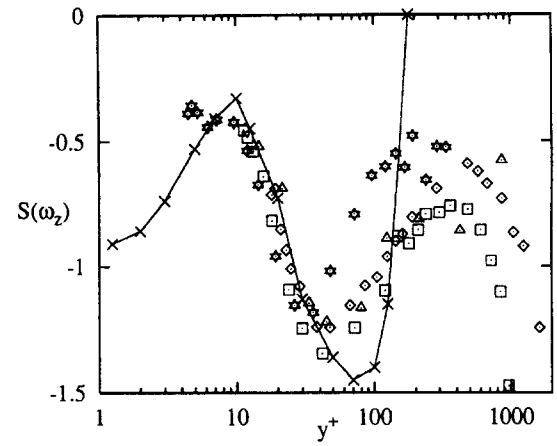

Figure 6 Spanwise vorticity skewness profiles versus y^+; data symbols same as in Figure 4

the channel flow profile of Kim et al. (1987) should not have this trend because of the confined nature of their flow. It is interesting to note that the $R_\theta = 1010$ mean velocity profile begins to deviate from the logarithmic law at about $y^+ = 120$. Thus, low Reynolds number effects on $\nu\omega'_z/u_\tau^2$ apparently penetrate closer to the wall than they do on $\Omega_z\nu/u_\tau^2$. Similar observations have also been made by Purtell et al. (1981) regarding low Reynolds number effects on u'/u_τ. Unlike the apparent damping effect on velocity fluctuations, increased viscous effects in the outer region with decreasing R_θ apparently amplify the ω_z fluctuations.

Figures 6 and 7 show profiles of $S(\omega_z)$ and $F(\omega_z)$, respectively. Included in these figures are the data of Balint et al. (1987) and the DNS results of Kim et al. (1987). A significant feature of the $S(\omega_z)$ distributions is the large negative peak reached near $y^+ = 40$. This feature is felt to be consistent with a process involving motions composed of high-intensity negative spanwise vorticity (of the same sign as the mean vorticity) moving outward from the sublayer. These motions may plausibly be associated with either the "head" portion of hairpin vortices, as, for example, studied by Lu and Smith (1988), and/or the shear layer-like motions observed in the physical simulations of Chu (1987) and computational database interrogation of Jimenez et al. (1988). Given these types of processes, the present skewness data indicate that, on average, the motions reach a maximum relative intensity near $y^+ = 40$. (Of course, the number of motions originating near the sublayer that actually reach a given y^+

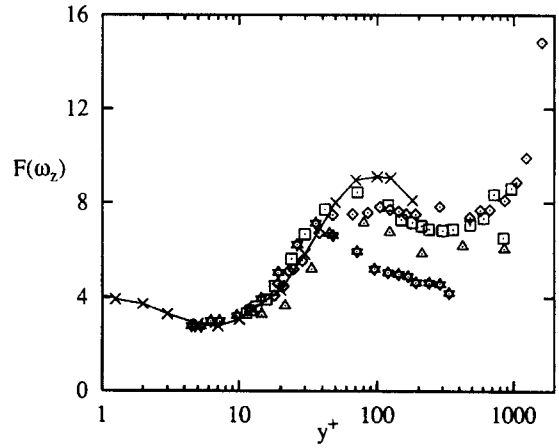

Figure 7 Spanwise vorticity flatness profiles versus y^+; data symbols same as in Figure 4

location and the presence of other motions composed of ω_z also influence $S(\omega_z)$.) This physical picture is also supported by the template-matching results of Lu and Smith (indicating $28 < y^+ < 32$ is the most probable region to observe a hairpin head) and the computational interrogation of Jimenez et al. (indicating that the tips of the shear layers tend to level-off near $y^+ = 35$).

The present $F(\omega_z)$ distributions of Figure 7 show very good agreement out to about the same y^+ location as the $S(\omega_z)$ profiles. The higher Reynolds number data continue, however, to exhibit good agreement for $y^+ > 50$, while the $R_\theta = 1010$ profile drops off to significantly smaller values. As with the skewness, the data of Balint et al. (1987) show very good agreement with the present results. In the outer region, their data ($R_\theta = 2100$) are also in agreement with the Reynolds number dependence indicated by the present results. The $F(\omega_z)$ profile of Kim et al. (1987) also shows excellent agreement with the present results for $y^+ \leq 50$. The increase in $F(\omega_z)$ with increasing y^+ in the near-wall region is also consistent with the existence of lifting sublayer motions. For example, as a vortical motion (say of scale about equal to the sublayer thickness and of characteristic vorticity u_τ^2/ν) moves rapidly outward from the sublayer, its relative scale will decrease and its relative circulation will increase with respect to the average surrounding motions. Such motions would contribute to increasingly intermittent ω_z fluctuations with increasing distance from the wall. Because a large flatness is generally regarded as an indication of intermittent behavior, the proposed physical process predicts that the $F(\omega_z)$ profile should increase for increasing y^+ values outside of the sublayer. At some distance from the wall, the probability of observing primarily shear layer-like motions is likely to significantly decrease. If motions originating near the sublayer characterize the $S(\omega_z)$ and $F(\omega_z)$ profiles out to this location, then at distances farther from the wall $F(\omega_z)$ should cease to increase, and $S(\omega_z)$ should cease to decrease. The increase in $S(\omega_z)$ for $y^+ > 40$ indicates that the pdf of ω_z becomes more symmetric. Combining this with the observation that the $F(\omega_z)$ profiles continue to increase for y^+ values significantly greater than 40 (at least at the higher Reynolds numbers), suggests that intermittent high-intensity motions associated with positive ω_z (of sign opposite that of the mean vorticity) become increasingly prevalent for $y^+ > 40$. Klewicki et al. (1990) have quantified the probability of observing positive $\tilde{\omega}_z$ in the wall region. For example, at $y^+ \approx 30$ there is a 20% probability observing positive $\tilde{\omega}_z$. * In addition, important connections between these positive ω_z motions and the transport of $\langle u^2 \rangle$ and $\langle uv \rangle$ have been identified (Klewicki et al. 1994).

Velocity gradient contributions to ω_z

The above results indicate that for $y^+ \leq 50$ the ω_z', $S(\omega_z)$ and $F(\omega_z)$ profiles are independent of R_θ when plotted in inner variables. From these results alone, however, we cannot comment on the relative contributions of the $\partial u/\partial y$ and $\partial v/\partial x$ velocity gradients, or whether these gradients individually follow inner variable scaling. In addition, the sign of the correlation between the underlying gradient combinations can be used to reveal whether the ω_z motions are, on average, more like a straining motion or are more akin to solid body rotation. That is, because $\omega_z = \partial v/\partial x - \partial u/\partial y$ and the 1, 2 strain rate component fluctuation is given by $s_{12} = 1/2(\partial v/\partial x + \partial u/\partial y)$, a positive correlation between $\partial u/\partial y$ and $\partial v/\partial x$ indicates a motion that is more straining than rotational, while a negative correlation indicates the opposite.

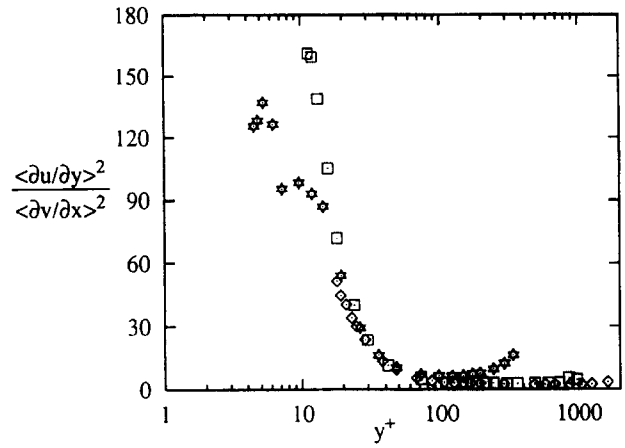

Figure 8 Ratio of the variance of $\partial u/\partial y$ to the variance of $\partial v/\partial x$ *versus* y^+; data symbols same as in Figure 2

The $\langle(\partial u/\partial y)^2\rangle/\langle(\partial v/\partial x)^2\rangle$ profiles of Figure 8 indicate that for all R_θ this ratio attains very large values in the buffer layer and is nearly constant across the logarithmic layer. In the wake region, the $R_\theta = 1010$ data exhibit a slight increase, while the higher R_θ data remain essentially constant. From this, we can conclude that for decreasing $y^+ < 50$ the $\tilde{\omega}_z$ motions are increasingly more like $\partial\tilde{u}/\partial y$ shear layers — especially when we factor in the rapid increase in $\partial U/\partial y$, see Figure 2. For increasing $y^+ > 50$, however, the instantaneous magnitudes of $\partial\tilde{u}/\partial y$ and $\partial\tilde{v}/\partial x$ have a much higher likelihood of being nearly equal. The more shear layer-like behavior of the $R_\theta = 1010$ wake region may result from the aforementioned direct effects of viscosity. The dominance of $\partial u/\partial y$ near the wall generally results in the $\partial u/\partial y$ statistical profiles to look very similar to those of ω_z. On the other hand, the rapid decrease in the $\langle(\partial u/\partial y)^2\rangle/\langle(\partial v/\partial x)^2\rangle$ ratio across the buffer layer is accompanied not only by a decrease in $(\partial u/\partial y)'$, but an increase in $(\partial v/\partial x)'$. This is shown by the $y^+ \approx 60$ peak in the inner normalized $(\partial v/\partial x)'$ profiles of Figure 9. As with $\nu\omega_z'/u_\tau^2$, these profiles suggest inner variable scaling for $y^+ < 120$ (the slight decrease in the peak value at $R_\theta = 4850$ a likely result of spatial resolution induced attenuation). In comparison with the DNS profile of Kim et al. (1987) (see Piomelli et al. 1989), the present profiles show essentially

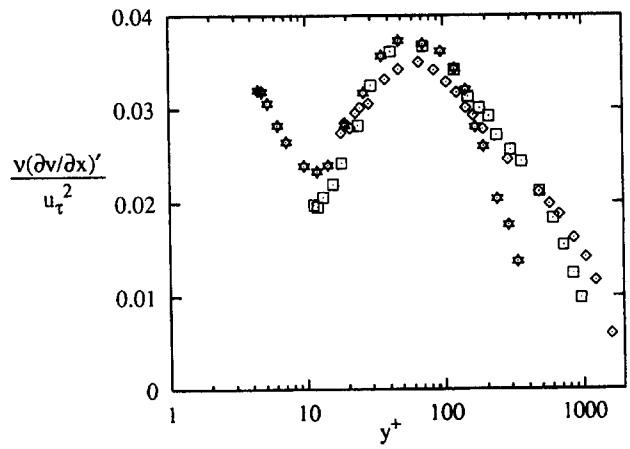

Figure 9 Inner variable normalized $\partial v/\partial x$ intensity profiles; data symbols same as in Figure 2

* Note that Figure 2 from Klewicki et al. (1990) incorrectly computed the cumulative probability of observing negative spanwise vorticity. At $y^+ = 30$, the data in this figure overestimate this probability by about 5% and at $y^+ = 40$ by about 10%.

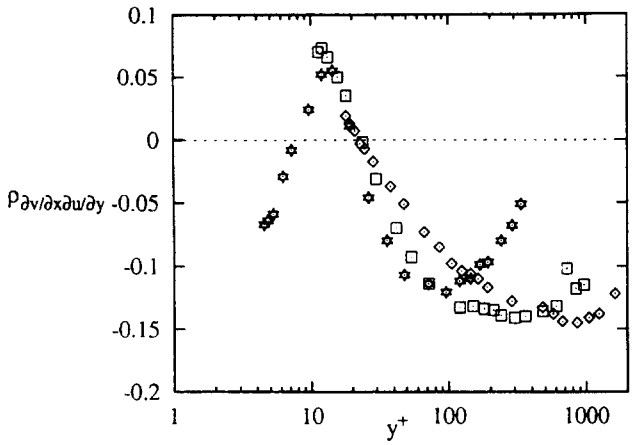

Figure 10 Correlation coefficient profile of $\partial v/\partial x$ and $\partial u/\partial y$ *versus* y^+; data symbols same as in Figure 2

the same shape, but are consistently about 10% larger in magnitude. The rapid increase of the $R_\theta = 1010$ profile for $y^+ < 10$ is, however, not exhibited by the profile of Kim et al. In this regard, it is worth noting that the nine-wire probe data of Balint shown in Piomelli et al. also exceed the DNS data near the wall. This feature may be associated with the breakdown in the validity of Taylor's hypothesis as the wall is approached (Piomelli et al.).

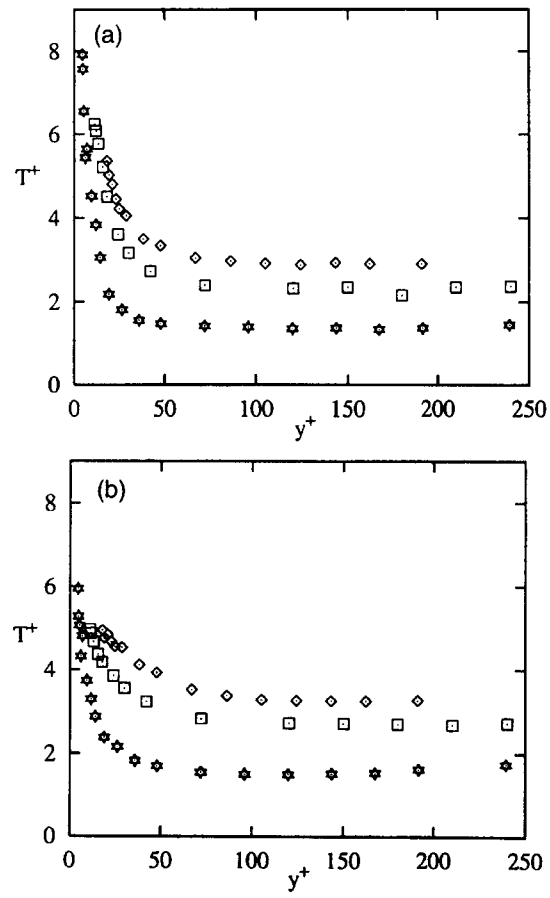

Figure 11 Inner normalized ω_z event durations *versus* y^+: a) positive events; b) negative events; data symbols same as in Figure 2; data derived for a signal conditioning amplitude equal to 1 rms

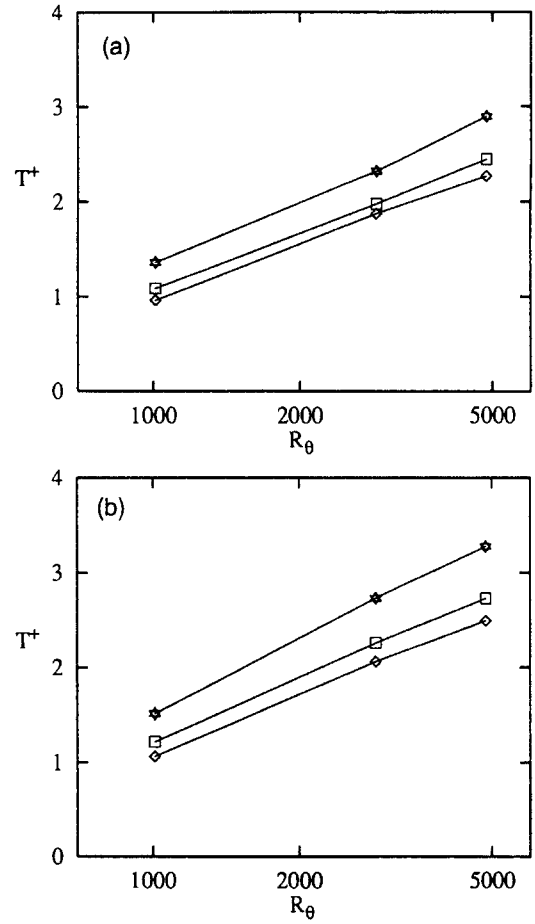

Figure 12 Inner normalized ω_z event durations *versus* R_θ and conditioning threshold at $y^+ \approx 120$: a) positive events; b) negative events; conditioning threshold = ω'_z, ✿; conditioning threshold = $2\omega'_z$, □, conditioning threshold = $3\omega'_z$, ◇

On the other hand, it is interesting to note that the $R_\theta = 1010$ profile diverges from the profile of Kim et al. at $y^+ \approx 12$, which happens to be equal to the streamwise grid resolution of the DNS study.

The $\rho_{\partial v/\partial x \partial u/\partial y}$ correlation coefficient profiles are shown in Figure 10. In examining these profiles, it is important to remember that the $R_\theta = 2870$ and 4850 data are affected by decreased probe resolution, which is likely to underly much of the deviation from the $R_\theta = 1010$ profile. (The Δz^+ spacings between the parallel- and x-arrays are about 16 and 26 at $R_\theta = 2870$ and 4850, respectively.) Even so, these data consistently indicate that the correlation is positive in the buffer region and displays a negative plateau across the logarithmic layer. We can, therefore, conclude that, on average, the (x, y) plane buffer layer motions have a slightly more straining rather than rotational character, while log layer motions tend to be more rotational than straining. Examination of the associated 2-D pdfs indicates that the positive buffer region correlations arise mostly from third quadrant $([-]\partial v/\partial x, [-]\partial u/dy)$ contributions, while the contributions to the negative log layer correlations are about equally shared between the second and fourth quadrants. Once again, because of the large mean gradient near the wall, the positive $\rho_{\partial v/\partial x \partial u/\partial y}$ is associated with negative $\partial u/\partial y$ that is predominantly positive $\partial \tilde{u}/\partial y$. On the other hand, the negative $\rho_{\partial v/\partial x \partial u/\partial y}$ values for $y^+ > 50$ are mainly associated with truly positive or negative $\tilde{\omega}_z$.

Spanwise vorticity time scales

Mixing length arguments contain the idea that the size of the eddies participating in the generation of the $\langle uv \rangle$ shear product display a monotone increase with distance from the wall. Semiempirical theories embodying these concepts (e.g., Prandtl 1925; Taylor 1932) generally rely on mean gradient transport notions to link the mean velocity field to the turbulent stresses. With regard to $\tilde{\omega}_z$, it is tempting to envision spanwise roller-like eddies of increasing diameter. Complicating this physical picture, however, are the existence of a near-wall $\tilde{\omega}_z$ field dominated by its $\partial\tilde{u}/\partial y$ gradient contribution, and the regularity of positive $\tilde{\omega}_z$ (counter to the notions of roller-type eddies and mean gradient transport respectively). In this context, it is therefore useful to explore the time scales of the ω_z fluctuations in the wall region.

The event duration analysis employed the same procedures as described in Klewicki et al. (1992). Therefore, only a brief synopsis is presented here. The analysis consisted of determining the duration of either positive or negative ω_z events conditioned on an event threshold amplitude. In addition, to account for amplitude deviations from an overall trend, events were sustained for a 20% drop below the peak event value even when the signal amplitude dropped below the threshold defining the beginning of the event. The threshold dependence of the detected event durations becomes very small for threshold levels greater than about 1 rms, ω'_z (see Figures 12a,b). For this reason, the data presentation below primarily employs a threshold equal to 1 rms. The 20% drop limit criterion, although somewhat arbitrary, was chosen based upon a compromise between being a relatively small fraction of the total signal amplitude, yet still having the effect of grouping a significant number of events. The purpose of the percentage drop limit is to account for the physical reality that turbulent events themselves contain fluctuations. Similar procedures have been used in other event detection techniques (e.g., Luchik and Tiederman 1987).

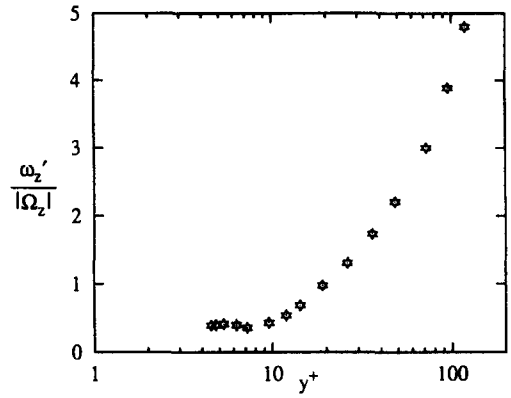

Figure 14 Spanwise vorticity intensity profile normalized by local mean vorticity magnitude

Figures 11a,b, respectively, show the mean ω_z event durations as a function of position from the wall in the inner region for positive and negative ω_z events. In each case, the mean event durations are normalized by inner variables. For y^+ greater than about 50, each R_θ distribution displays a different but essentially constant value. Note also that since the convection velocity of inner region eddies is nearly constant at about $0.6U_\infty$, the event durations in Figures 11a,b correspond to nearly constant convected lengths as well. Comparison between the like R_θ curves of Figures 11a,b indicates that in the viscous sublayer, positive event durations reach larger values than the negative durations. In the constant event duration region, however, the mean negative event durations are slightly but consistently larger than the positive event durations. The significant increase in the negative event durations in the buffer region is likely a consequence of the lifting streamwise shear layer-like motions populating this region. On the other hand, the very sharp rise in the positive event durations for $y^+ < 15$ (exceeding that of the negative events) is

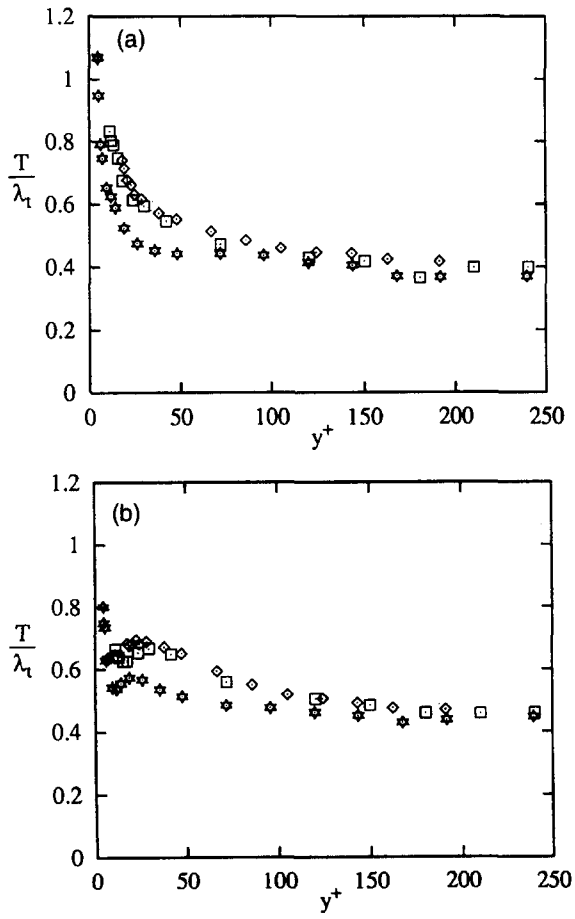

Figure 13 ω_z event durations normalized by the Taylor time scale *versus* y^+: a) positive events; b) negative events; data symbols same as in Figure 2

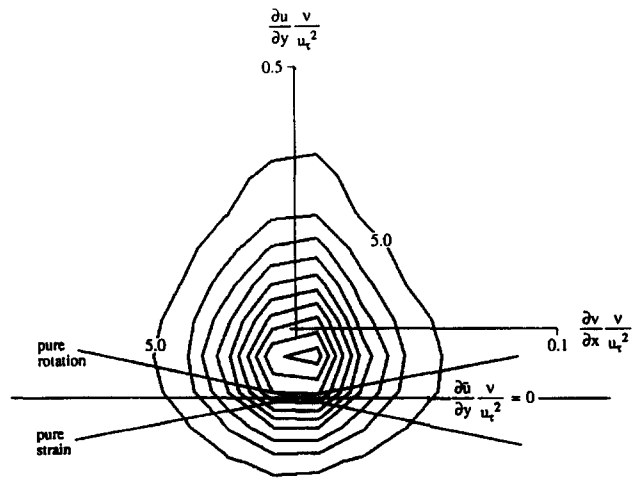

Figure 15 Joint pdf of the velocity gradients contributing to ω_z at $y^+ = 26.3$

probably associated with sublayer streaks. That is, because of the no-slip condition there is a strong negative correlation between u and ω_z in the vicinity of the sublayer, and thus, low-speed sublayer streaks may be reliably associated with positive ω_z fluctuations (Klewicki et al. 1994).

Very distinct R_θ dependencies are indicated in both Figures 11a and 11b. Even very near the surface both the positive and negative data exhibit increasing event durations at a fixed y^+ value with increasing R_θ. In addition, the near-wall position where the sharp increase in event duration occurs is at a larger y^+ value with increasing R_θ. These features may, in fact, be linked to the increasing magnitude and position of u'/u_τ with increasing R_θ (e.g., Klewicki and Falco 1990) and may also be associated with the apparently significant changes in near-wall vorticity stretching and reorientation with increasing R_θ (e.g., Wei and Willmarth 1989; Antonia and Kim 1994). Comparison of the present results for $y^+ > 50$ with the outer region data of Klewicki et al. (1992) indicates that for fixed R_θ the event durations remain essentially constant to the edge of the boundary layer. Therefore, this previous result showing a decrease in event durations under outer normalization also holds for the present data. Comparison of the relative magnitudes between the different R_θ profiles indicates that the positive and negative event durations exhibit the same rate of increase with increasing R_θ. Figures 12a,b explicitly demonstrate this feature by plotting the event durations at $y^+ \approx 120$ *versus* R_θ. In addition, Figures 12a,b plot event durations derived by using different conditioning thresholds. These results show that the R_θ dependence is independent of threshold for thresholds greater than about 1 rms. Both the positive and negative event durations exhibit a nearly logarithmic dependence on R_θ.

The results of Figures 11a,b indicate that at a given R_θ, the motions bearing ω_z outside the buffer region are essentially of fixed time scale. These data, therefore, do not suggest a hierarchy of significantly increasing $\tilde{\omega}_z$ eddy sizes with increasing distance from the wall. In contrast, they do support observations that outside the sublayer the $\tilde{\omega}_z$ motions most directly involved in transport are intermediate in scale (e.g., Falco 1974, 1977, 1983, 1991; Murlis et al. 1982; Head and Bandyopadhyay 1981; Bandyopadhyay and Balasubramanian 1995). In particular, Falco

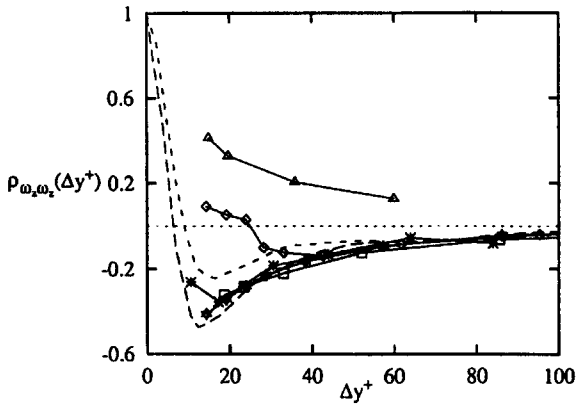

Figure 16 Correlation coefficient profiles as a function of inner normalized wall-normal probe separations (Rajagopalan and Antonia 1993, $-\rho_{u\omega'_z}$ reference probe at $y^+ = 4.75$, $R_\theta = 1450$, *; Kim [from Rajagopalan and Antonia], $-\rho_{u\omega'_z}$ reference probe at $y^+ = 4.75$, $R_\theta = 280$, — —; Antonia and Kim 1994, reference probe at $y^+ = 15.0$, $R_\theta = 660$, -----; present, reference probe at $y^+ = 7.5$, ✿; present, reference probe at $y^+ = 13.4$, □; present, reference probe at $y^+ = 29.5$, ◇; present, reference probe at $y^+ = 100.5$, △)

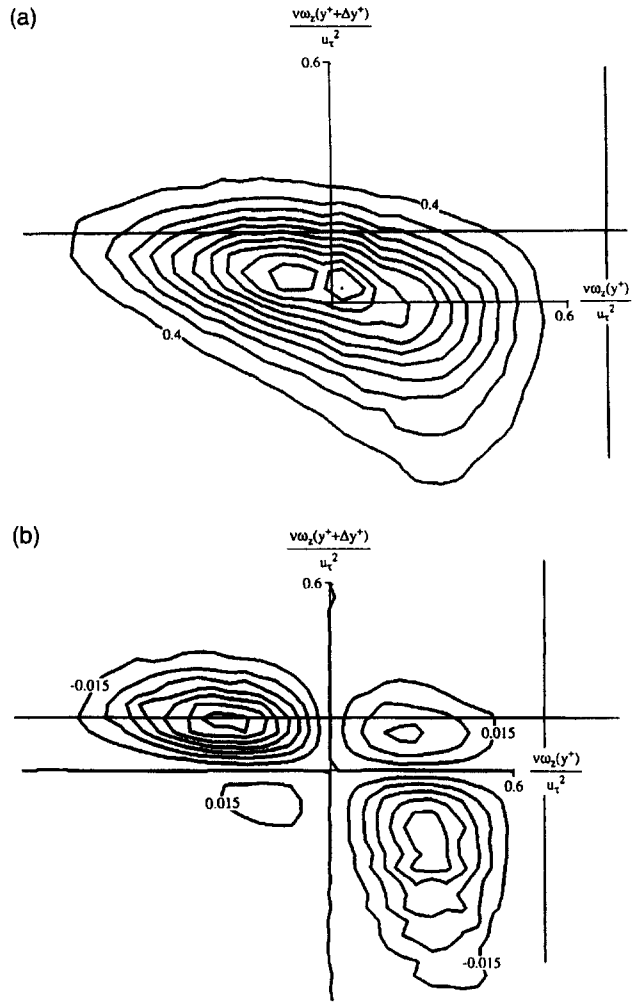

Figure 17a Joint pdf of spanwise vorticity for reference probe at $y^+ = 7.5$ and a probe separation of $\Delta y^+ = 14.4$; for this and all subsequent pdfs, labeled axes are referenced to ω_z origin, while unlabeled axes are referenced to $\tilde{\omega}_z$ origin

Figure 17b Weighted joint pdf corresponding to the pdf of Figure 6a; note that the weighting is performed using magnitudes referenced to ω_z (labeled) axes

has suggested that these motions are comparable in size to Taylor's microscale. To explore this notion further, the y^+ distribution of the Taylor time scale (e.g., Tennekes and Lumley 1972)

$$\lambda_t = \sqrt{\frac{2\langle u^2 \rangle}{\langle (\partial u/\partial t)^2 \rangle}}$$

was computed at each Reynolds number and subsequently used to normalize the data of Figures 11a,b. These results are displayed in Figures 13a,b, respectively. As can be seen, this normalization results in the two higher R_θ distributions to merge at positions well within the buffer region and outside the buffer region, generates an apparently invariant curve for all three R_θ. Obviously, we can also derive from this that the inner normalized Taylor time scale profiles look very similar to the event duration profiles of Figure 11.

The model of turbulence production proposed by Falco (1991) explicitly includes coherent motion interactions consistent with

the above event duration results. In particular, this model describes buffer-layer physics in terms of logarithmic region eddies of intermediate scale that convect toward the wall and perturb/rearrange the highly distributed, shear dominated, sublayer vorticity field. In the context of this model, it is also interesting to note that numerous studies (e.g., Gad-el-Hak and Bandyopahdyay 1994) have found R_θ dependencies in inner region u'/u_τ, v'/u_τ and $\langle uv\rangle/u_\tau^2$ profiles. The apparent R_θ invariance of the inner normalized near-wall ω_z statistical profiles shown herein are, therefore, felt to indicate that the motions resulting from and involved in the redistribution of sublayer vorticity are on average universal in their ω_z content, but are not universal in their capacity to generate turbulent stresses. The event duration results suggest that these changes are likely to be associated with the observed R_θ variations in the inner normalized scale of the log-layer ω_z eddies relative to the thickness of the viscous sublayer. In turn, this suggests that the fate of these Taylor scale eddies at high Reynolds number may in large part determine the R_θ dependence of inner region structure. In connection with this, Falco (1991) provides evidence that these eddies tend to be vortex ring-like in nature, and with increasing R_θ, may undergo wavy core instability. Similarly, Bandyopadhyay and Balasubramanian (1995) provide evidence that the so-called vortex Reynolds number $R_\Gamma(\equiv \Gamma/\nu$, where Γ is the circulation of a vortex) of log-layer eddies strongly affects long time statistical structure. Because of the weak dependence of ω_z event duration on signal conditioning threshold, a reasonable estimate for R_Γ is obtained from $\pi/4L_c^2\omega_z'/\nu$, where L_c is the convected length scale associated with the event durations of Figures 11a,b. L_c computed using a convection velocity of $0.6U_\infty$ for positive ω_z eddies at $y^+\approx 50$ yields $R_\Gamma = 58$, 92, and 167 at $R_\theta = 1010$, 2870, and 4850, respectively. These estimates, therefore, suggest a strong R_Γ dependence on R_θ. The source of this increase comes from the event duration increase shown in Figures 11a,b, as well as a small relative increase in U_c^+ ($\equiv 0.6U_\infty^+$) with increasing R_θ.

Two-point results

Information derived from the instantaneous correlations of spanwise vorticity at two points are presented for probe separations in both the y (wall-normal) and z (spanwise) directions. In the former case, the reference (fixed) probe is positioned at a given

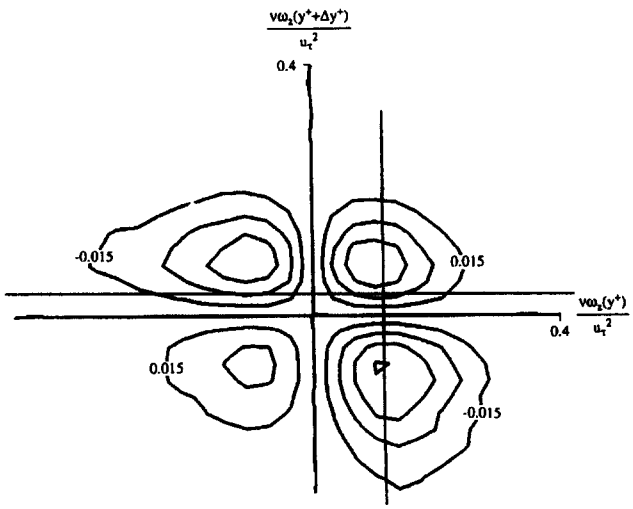

Figure 18 Weighted joint pdf of spanwise vorticity for reference probe at $y^+ = 29.5$ and a probe separation of $\Delta y^+ = 42.6$

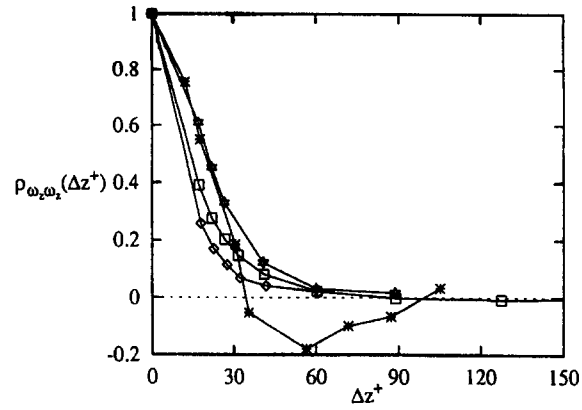

Figure 19 Correlation coefficient profiles as a function of inner normalized spanwise probe separations (Kreplin and Eckelmann 1979, probes at $y^+ = 0.0$, $R_\theta \approx 300$, $*$; present, probes at $y^+ = 6.7$, ✿; present, probes at $y^+ = 15.3$, ⊡; present, probes at $y^+ = 33.3$, ◇)

(x, y, z) location, and its signal is correlated with a movable probe having the same x and z coordinates but varying y position. For these correlations, the movable probe is always at a greater y value than the reference probe. Wall-normal correlations were performed for reference probe positions at $y^+ = 7.5$, 13.4, 29.5, and 100.5. The second type of probe arrangement involved maintaining the same x and y coordinates of the movable probe but varying its z position. These spanwise correlations were acquired at $y^+ = 6.7$, 15.3, and 33.3.

During the correlation experiments, the wind-tunnel freestream dynamic pressure was adjusted to match the $R_\theta = 1010$ condition of the single-probe measurements. An independent determination of u_τ was, however, not made. For this reason, the correlation experiments are identified as being at Reynolds number $R_\theta \approx 1010$. To explore this assumption, mean and rms velocity data from the two experiments were compared by normalizing the data from the two probe experiments with the $R_\theta = 1010$ friction velocity. These data compared favorably. In addition, as an even more stringent test (because u_τ is squared), the moving probe $v\omega_z'/u_\tau^2$ data were superimposed on the $R_\theta = 1010$ $v\omega_z'/u_\tau^2$ profile of Figure 4 (Klewicki 1989). Once again, the same u_τ value was used to normalize both datasets. This comparison indicated that the correlation data follow the single-probe profile quite closely, although there was some scatter. This scatter, however, was not correlated with the probe separation distance and, thus, could not be reliably attributed to biases caused by probe interference effects. Overall, the level of agreement was deemed sufficient to justify using the $R_\theta = 1010$ u_τ value.

On interpreting spanwise vorticity correlations

Unlike the streamwise and wall-normal components, the spanwise vorticity component has a significant mean value, $\Omega_z \approx -\partial U/\partial y$. Thus, in order to correctly interpret ω_z correlations in the context of instantaneous motions, we must take into account the mean vorticity at any given location. In connection with this, Figure 14 shows the ratio of the $R_\theta = 1010$ $v\omega_z'/u_\tau^2$ data to Van Driest's (1956) Ω_z profile shown in Figure 2. For y^+ less than about 20, Ω_z has a magnitude greater than one rms. Thus, nearer the wall, positive ω_z fluctuations must be quite large to constitute positive $\tilde{\omega}_z$. On the other hand, farther from the wall, the fluctuations alone increasingly take on the character of the instantaneous spanwise vorticity. In the pdfs presented below, axes centered about $\tilde{\omega}_z = 0$ and $\omega_z = 0$ are given. This allows the true instantaneous vorticity content associated with a given fluctuation level to be better understood.

The large mean component of $\tilde{\omega}_z$ in the near-wall region also has significance regarding the nature of the instantaneous motions bearing the velocity gradients contributing to $\tilde{\omega}_z$. Previously, we explored whether the velocity gradient contributions to ω_z represent shear-layer-like motions, motions bearing nearly solid-body rotation, or motions close to pure strain. This was done by examining the characteristics of the 2-D pdf associated with the $\partial v/\partial x$ and $\partial u/\partial y$ fluctuations. It is now useful to re-examine this issue in the context of $\tilde{\omega}_z$ contributions. In particular, consider the $(\partial v/\partial x, \partial u/\partial y)$ pdf at $y^+ = 26.3$ shown in Figure 15, and note the shift in the position of the pdf relative to the line specifying $\partial\tilde{u}/\partial y = 0$. (Because of the large downstream development of this boundary layer, $\partial\bar{v}/\partial x$ exhibited an essentially zero mean value.) Also, note that the $\partial v/\partial x$ axis extends to only 1/5 the value of the $\partial u/\partial y$ axis. From Figure 15, it is readily seen that the greatest fraction of $\partial\tilde{u}/\partial y$ is positive, although the negative fraction is not negligible. Similar to what was earlier noted for the fluctuations, motions comprising pure rotation and pure strainrate in a absolute sense may be identified on Figure 15 by recalling that $\tilde{s}_{12} = 1/2(\partial\tilde{v}/\partial x + \partial\tilde{u}/\partial y)$ and $\tilde{\omega}_z = \partial\tilde{v}/\partial x - \partial\tilde{u}/\partial y$. From these definitions it is readily apparent that positive $\partial u/\partial y$ is always associated with motions most like a $\partial\tilde{u}/\partial y$ shear layer, while negative $\partial u/\partial y$ (but positive $\partial\tilde{u}/\partial y$) has a significantly enhanced probability of being associated with motions close to pure rotation (negative $\tilde{\omega}_z$) or pure strain (positive $\tilde{s}_{12}$). On the other hand, because of the significant mean component of $\partial\tilde{u}/\partial y$, strongly negative $\partial u/\partial y$ generally constitutes only weakly negative $\partial\tilde{u}/\partial y$. Negative $\partial\tilde{u}/\partial y$ is, therefore, relatively likely to occur in conjunction with a $\partial\tilde{v}/\partial x$ gradient of similar magnitude. Thus, motions close to either pure rotation (positive $\tilde{\omega}_z$) or pure strain (negative $\tilde{s}_{12}$) are relatively more likely for the condition of negative $\partial\tilde{u}/\partial y$ than for positive $\partial\tilde{u}/\partial y$. Conversely, negative $\partial\tilde{u}/\partial y$ has a relatively smaller chance of being part of a shear layer type of motion composed of either $\partial\tilde{v}/\partial x$ or $\partial\tilde{u}/\partial y$.

Wall-normal probe separation correlations

The correlation coefficient profiles for wall-normal probe separations are shown in Figure 16. Also included in Figure 16 are the $\rho_{\omega_z\omega_z}$ and $\rho_{u\omega_z}$ data reported in Rajagopalan and Antonia (1993), and the $\rho_{\omega_z\omega_z}$ data of Antonia and Kim (1994). As can be seen, the correlations for the reference probe at $y^+ = 7.5$ and 13.4 display large negative values, even for the smallest probe separations. (Recall, that these correlation coefficients, by definition, have a value of 1.0 at $\Delta y^+ = 0$.) The present results for reference probe at $y^+ = 7.5$ and the DNS results for reference position of $y^+ = 4.75$ display good agreement, as does the $\rho_{u\omega_z}$ correlation profile of Rajagopalan and Antonia (for stationary single wire probe at $y^+ = 4.75$).

The DNS data in Figure 16 indicate that moving the reference position from $y^+ = 4.75$ to 15 results in the maximum negative correlation magnitude to decrease from about -0.475 to -0.245, and the relative position of the peak to move outward from Δy^+ near 12.5 to Δy^+ near 16.5. While the present correlations for stationary probe at $y^+ = 7.5$ show good agreement with the DNS correlations referenced to $y^+ = 4.75$, the present correlations for fixed probe at $y^+ = 13.4$ display significantly larger negative magnitudes than the DNS data referenced to $y^+ = 15.0$. In fact, the present curves at $y^+ = 7.5$ and 13.4 are nearly identical, although given the limited amount of experimental data, we cannot say whether a change in peak position exists. On the other hand, the present curve for stationary probe at $y^+ = 29.5$ exhibits features generally consistent with the trends displayed by the DNS data. In particular, the peak negative value has decreased to -0.14 and has moved outward to a relative probe position of $\Delta y^+ = 42.6$. For greater Δy^+ probe separations, the present curves for fixed probe at $y^+ = 7.5$ 13.4 and 29.5 merge. For fixed probe at $y^+ = 100.5$, the existence of a negative peak disappears. Even for this case, however, the nonzero extent of the correlation remains essentially the same as for correlations with fixed probe in the viscous sublayer or buffer region.

Contributions underlying the correlations shown in Figure 16 may be revealed by exploring the properties of the 2-D $\omega_z(y^+)$, $\omega_z(y^+ + \Delta y^+)$ pdfs and their associated weighted pdfs. The weighted pdfs, or quadrant contributions, are computed (for example) by multiplying the probability of measuring a $\omega_z(y^+)$, $\omega_z(y^+ + \Delta y^+)$ combination with the value of the given $\omega_z(y^+)$ $\omega_z(y^+ + \Delta y^+)$ product. Thus, the weighted pdf graphically reveals the statistically most significant motions underlying any given correlation. Those associated with the point of closest separation in the correlation profile with reference probe at $y^+ = 7.5$ are shown in Figures 17a,b, respectively. These pdfs are shown relative to inner normalized coordinate axes (as opposed to axes normalized by the local rms values) in order to reflect the rapid decrease in the ω_z fluctuations with increasing distance from the wall. As mentioned previously, these pdfs are plotted relative to coordinate axes centered about $\omega_z = 0$ (labeled) as well as axes centered about $\tilde{\omega}_z = 0$ (unlabeled). Note also that the weighted pdfs were constructed using ω_z rather than $\tilde{\omega}_z$. The shape of the pdf in Figure 17a indicates that significant contributions to the negative correlation come from both the second and fourth quadrants. This is illustrated even more clearly in the weighted pdf (Figure 17b), which shows that the contributions from the second quadrant outweigh those from the fourth quadrant. Second quadrant contributions correspond to positive ω_z being present at the upper probe ($y^+ = 21.9$) and negative ω_z being present at the lower probe. For the upper probe, this quadrant corresponds to either weakly negative $\tilde{\omega}_z$ (i.e., negative but having magnitude less than Ω_z) or positive $\tilde{\omega}_z$ (i.e., of sign opposite Ω_z). The position of the total vorticity axis indicates that about half of the contributions to the second quadrant constitute positive $\tilde{\omega}_z$. For the lower probe, however, the second quadrant always corresponds to negative $\tilde{\omega}_z$ of magnitude greater than the mean. Similarly, regarding the fourth quadrant, the position of the $\tilde{\omega}_z = 0$ axes indicates that the lower probe motions entirely constitute negative $\tilde{\omega}_z$ of magnitude smaller than the mean, while by definition the upper probe is always sensing negative $\tilde{\omega}_z$ having magnitude greater than the mean. Relative to the positive contributions, the quadrant three results of Figure 17b indicate that negative ω_z at both probes is a rare condition.

Weighted pdfs associated with the other correlations in Figure 16 have also been examined. These revealed important changes with y^+ regarding the source of the negative peak in the near-wall correlations. In contrast with Figure 17b, Figure 18 shows that the negative peak at $y^+ = 29.9$ has nearly equal contributions from the second and fourth quadrants. Furthermore, almost all of the contributions to the second quadrant come from positive $\tilde{\omega}_z$ at the upper probe, while the lower probe now senses significant positive $\tilde{\omega}_z$, as well. The simultaneous presence of negative ω_z at both probes is also not nearly as rare as it was for reference probe at $y^+ = 7.5$. Examination of the weighted pdf corresponding to the negative peak in the correlation for reference probe at $y^+ = 13.4$ (not shown), indicates that the transition between Figures 17b and 18 occurs smoothly. Because of the large decrease in $\partial U/\partial y$ from $y^+ = 7.5$ to 29.9, however, the relative increase in positive $\tilde{\omega}_z$ at the lower probe is more significant. As evidenced by the axes referenced to $\tilde{\omega}_z$, much of the first quadrant contributions in Figure 18 involve positive $\tilde{\omega}_z$ sensed at both probes, while both of the negative quadrant contributions largely arise from truly counter-rotating motions.

In contrast to the near-wall results, the correlation with reference probe at $y^+ = 100.5$ does not show a negative excursion. The weighted pdfs in this case (not shown) indicate that the positive correlation results from nearly equal first and third quadrant contributions. Interestingly, first quadrant events are

more frequent, but third quadrant events have larger maximum magnitude. In addition, because $|\Omega_z|$ is only about 25% of ω'_z at $y^+ = 100$, the like-sign ω_z combinations leading to the positive correlation are almost always like-sign $\tilde{\omega}_z$ as well. Finally, the decrease in this correlation with increasing Δy^+ must arise from increased quadrant two and four contributions. Therefore, for probe separations greater than our largest separation of 60 Δy^+ the two probes will often instantaneously sense opposing sign $\tilde{\omega}_z$.

Spanwise probe separation correlations

Correlation coefficient profiles for spanwise probe separations are shown in Figure 19. Unlike the wall-normal results, across the buffer region these correlations display no significant negative excursions. This is taken to indicate the general predominance of like sign ω_z eddies. In this regard, the results at $y^+ = 6.7$ are somewhat surprising when contrasted with the $\rho_{\partial u/\partial y \partial u/\partial y}(\Delta z^+)$ correlations of Kreplin and Eckelmann (1976) at $y^+ = 0$. That is, because of the dominance of the $\partial u/\partial y$ gradient contribution to ω_z in and near the viscous sublayer, the correlation of this gradient at the wall was expected to be very similar to those of ω_z near the edge of the sublayer. Evidently, however, the instantaneous flow features generating the significant negative values in the correlation of Kreplin and Eckelmann are no longer reflected in an average sense at a distance corresponding to $y^+ = 6.7$ from the surface. At each y^+ location, all of the correlations in Figure 10 drop to negligible values for Δz^+ probe separations greater than about 60. Thus, as with the Δy^+ results, these correlations suggest that the underlying contributions are spatially compact. On the other hand, for $\Delta z^+ < 60$, the shape of the correlation profiles at differing y^+ are distinctly different. Specifically, these data indicate an increasing spatial coherence with decreasing distance from the wall. These results also support the notion that the organized ω_z motions become increasingly distributed in z with decreasing y^+.

The weighted pdfs associated with the smallest (nonzero) Δz^+ separations at $y^+ = 6.7$ and 33.3 in Figure 19 are shown in Figures 20 and 21. For a 2-D flow, pdfs of Δz^+ correlations should be symmetric about a 45° line bisecting the first and third quadrants. As is evident, the pdfs in Figures 20 and 21 display this feature. Because measurement biases resulting from probe interference effects would cause deviations from this feature, Figures 20 and 21 are felt to provide a further indication that such biases were not present. The results at $y^+ = 6.7$ show that like sign ω_z is almost always observed at the two probes.

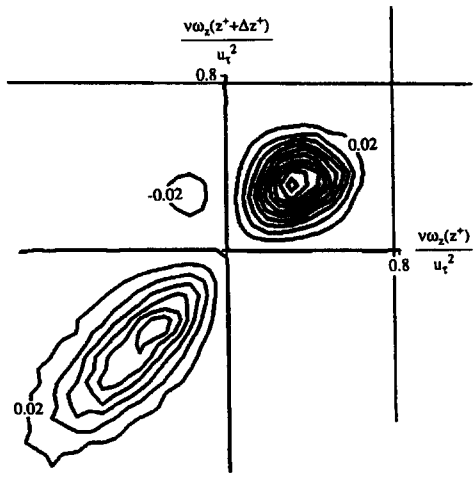

Figure 20 Weighted joint pdf of spanwise vorticity at $y^+ = 6.7$ and a probe separation of $\Delta z^+ = 17.0$

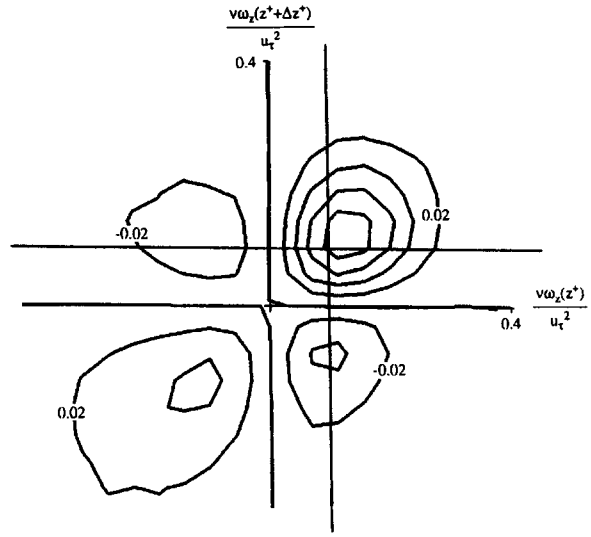

Figure 21 Weighted joint pdf of spanwise vorticity at $y^+ = 33.3$ and a probe separation of $\Delta z^+ = 18.0$

Generally consistent with the negatively skewed single point pdf, first quadrant contributions are significantly more prevalent, while third quadrant contributions regularly reach much larger magnitudes. In the context of sublayer physics, first quadrant motions are likely to be highly represented by streaks, while third quadrant motions are largely resultant from hairpin vortex and/or shear-layer-like motions. When viewed relative to the $\tilde{\omega}_z$ axis, the weighted pdf in Figure 20 indicates that its associated pdf lies almost entirely in the third quadrant. Thus, the first and third quadrants in the weighted pdf (about the ω_z axes) distinguishes only between negative $\tilde{\omega}_z$ having magnitude less than and greater than Ω_z, respectively. The effect of the decreasing mean velocity gradient with increasing y^+ is to shift the $[\tilde{\omega}_z(z^+), \tilde{\omega}_z(z^+ + \Delta z^+)]$ origin toward the $[\omega_z(z^+), \omega_z(z^+ + \Delta z^+)]$ origin along the 45° line bisecting the first quadrant. Regarding this, the weighted pdf at $y^+ = 15.3$ (not shown) indicates that the condition of opposing sign ω_z at the two probes is rare. As a direct consequence of the shift of the $\tilde{\omega}_z$ origin toward the ω_z origin, however, the $y^+ = 15.3$ weighted pdf also indicates that opposing sign $\tilde{\omega}_z$ at the two probes occurs with significant regularity. The further translation of the $\tilde{\omega}_z$ axes toward the ω_z origin in Figure 21 ($y^+ = 33.3$) indicates that as the probes traverse through buffer region the greatest contributor to the positive correlation shifts from negative $\tilde{\omega}_z$ at the two probes to positive $\tilde{\omega}_z$ at the two probes.

Summary and discussion

The present results indicate that for y^+ less than about 50 and under inner variable normalization the statistical moment profiles of ω_z (up to flatness) merge over the given R_θ range. With regard to ω'_z, inner scaling holds to significantly greater y^+ values. These results agree with the very low R_θ channel flow computations of Antonia and Kim (1994), indicating an invariant inner normalized profile shape for $y^+ > 12$. (It is also interesting to contrast these results to existing high resolution u'/u_τ, v'/u_τ and $\langle uv \rangle / u_\tau^2$ data, which display significant R_θ variations (e.g., Wei and Willmarth 1989; Klewicki and Falco 1990; Klewicki et al. 1994) in the buffer and logarithmic regions.) Because of our inability to obtain ω'_z measurements closer to the wall for $R_\theta > 1010$, we were not able to confirm the R_θ increase Antonia and Kim observed for sublayer $\nu\omega'_z/u_\tau^2$. Outside the logarithmic

region, the $R_\theta = 1010$ $\nu\omega_z'/u_\tau^2$ values deviated significantly from the two higher R_θ profiles. It is hypothesized that this feature has association with the significant changes in wake region structure known to occur for $R_\theta < 3000$.

When normalized by either inner or outer variables, the ω_z event duration profiles at different Reynolds numbers failed merge. Normalization by the Taylor time scale, however, resulted in the three profiles to define a single curve for y^+ values outside the buffer region. This result argues quite strongly against the notion of a hierarchy of scales of organized ω_z motions populating the logarithmic and outer layers. In terms of ω_z, the present results provide a basis for modeling the boundary in terms of only two scales of motion. In and near the viscous sublayer, the motions have a high aspect ratio from being elongated in the streamwise direction. On the other hand, from the outer edge of the buffer layer to the edge of the boundary layer, the motions are spatially compact and have characteristic duration corresponding to the Taylor time scale. The spatial correlation results in the logarithmic region reinforce the notion that the ω_z bearing motions tend to be spatially compact and of intermediate scale. Furthermore, analysis of log region $\rho_{\partial v/\partial x \partial u/\partial y}$ correlations indicated that $\tilde{\omega}_z$ motions of this region have a higher likelihood of being akin to solid body rotation (as opposed to pure strain or shear layer-like), and with increasing y^+, these motions are about as likely to constitute positive $\tilde{\omega}_z$ as negative $\tilde{\omega}_z$.

The analysis of the joint pdfs underlying the correlations indicated the prevalence of organized positive ω_z (and in many cases positive $\tilde{\omega}_z$) in the wall region. In particular, the pdfs associated with the strongly negative wall-normal correlations with reference probe at $y^+ = 7.5$ and 13.4 reveal that when positive $\tilde{\omega}_z$ is in the upper portion of the buffer region there is a high probability that strongly negative ω_z will be present in the sublayer and lower buffer region. The influence of positive $\tilde{\omega}_z$ in the buffer layer has been proposed by Falco (1983, 1991) as representing an important initiating mechanism for the redistribution of sublayer vorticity and subsequent production of new turbulence. Conversely, these same pdfs show that when negative ω_z is sensed in the upper portion of the buffer layer, there is a high likelihood of observing positive ω_z (and at $y^+ = 13.4$, positive $\tilde{\omega}_z$) closer to the wall. This arrangement of spanwise vorticity corresponds closely to the eruptive ejection-like phenomenon that occurs under the "head" portion of hairpin-like vortices, as described by Smith et al. (1991). They identify this eruptive behavior with significant Reynolds stress production. In connection with the relative contributions of $\partial v/\partial x$ and $\partial u/\partial y$, the turbulent events described by Falco (1991) and Smith et al. are associated with the magnitude ranges of ω_z, which have the highest likelihood of representing motions near solid body rotation (i.e., positive $\tilde{\omega}_z$, or positive ω_z but weakly negative $\tilde{\omega}_z$). These results are consistent with the analysis of Klewicki et al. (1994) indicating the importance of motions bearing positive ω_z in both the generation of $\partial\langle uv\rangle/\partial y$ and the vertical transport of $\langle u^2\rangle$.

Klewicki et al. (1990) provide a physical interpretation of single point ω_z pdfs based upon the solenoidality of the vorticity field. This lead to two conjectures regarding the coherent arrangements of boundary-layer vorticity filaments: (1) vorticity filaments in and near the sublayer generically comprise global loops that circumscribe the surface in a manner similar to those lying in the wall itself; and (2) sufficiently far from the wall, the generic arrangement of filaments comes in the form of locally formed loops that are, in general, highly three dimensional (3-D). In the region between (i.e., the buffer region), there is envisioned to exist a mix of locally perturbed global loops (e.g., the perturbed portions being hairpin-like vortices) and the smaller scale 3-D loops. The features of the present correlations with Δz^+ separation agree with these notions. In addition, the shift to positive ω_z contributions from both probes with increasing y^+ further supports the assertion that hairpin-like/shear-layer vortices are predominantly confined to the region $y^+ \leq 50$. Finally, the disappearance of the negative peak in the wall-normal correlations with increasing distance from the wall is expected because there is an increased range of orientations that the locally formed loop-like motions may attain with respect to a fixed probe pair. On the other hand, because of the large mean contribution to $\tilde{\omega}_z$ nearer the wall, opposing sign $\tilde{\omega}_z$ combinations are likely to arise because of the predictable perturbing effect that strongly positive or negative $\tilde{\omega}_z$ bearing motions positioned in the buffer region have on sublayer $\tilde{\omega}_z$ (see also, Rajagopalan and Antonia 1993; Klewicki et al. 1994).

Acknowledgment

This work was partially supported by the Air Force Office of Scientific Research, contract number 87-0047, J. McMichael was the contract monitor.

References

Alfredsson, P. H., Johansson, A. V., Haritonidis, J. H. and Eckelmann, H. 1988. The fluctuating wall-shear stress and velocity field in the viscous sublayer. *Phys. Fluids*, **31**, 1026–1033

Antonia, R. A. and Kim, J. 1994. Low-Reynolds-number effects on near-wall turbulence. *J. Fluid Mech.*, **276**, 61–80

Antonia, R. A., Rajagopalan, S., Subramanian, C. S. and Chambers, A. J. 1982. Reynolds number dependence of the structure of a turbulent boundary layer. *J. Fluid Mech.*, **121**, 123–140

Balint, J. L., Vukoslavcevic, P. and Wallace, J. M. 1987. A study of the vortical structure of the turbulent boundary layer. In *Advances in Turbulence*, G. Comte-Bellot and J. Mathieu (eds.), Springer-Verlag, New York, 456–464

Bandyopadhyay, P. R. and Balasubramanian, R. 1995. Vortex Reynolds number in turbulent boundary layers. *Theoret. Comput. Fluid Dynamics*, **7**, 101–117

Bernard, P. S., Thomas, J. M. and Handler, R. A. 1993. Vortex dynamics and the production of Reynolds stress. *J. Fluid Mech.*, **276**, 385–419

Böttcher, J. and Eckelmann, H., 1985. Measurement of the velocity gradient with hot-film probes. *Exp. Fluids*, **3**, 87–91

Browne, L. W. B., Antonia, R. A. and Chua, L. P. 1989. Calibration of *x*-probes for turbulent flow measurements. *Exp. in Fluids*, **7**, 201–208

Chu, C. C. 1987. A study of turbulence production and modification in boundary layers using a new photochromic visualization technique. Ph.D. dissertation, Michigan State University, East Lansing, MI, USA

Coles, D. E. and Hirst, E. A. 1969. *Proc. 1968 AFOSR-IFP-Stanford Conference on Computation of Turbulent Boundary Layers*, Stanford University, Stanford, CA, USA

Falco, R. E. 1974. Some comments of turbulent boundary-layer structure inferred from the movements of a passive contaminant. AIAA Paper 74-99

Falco, R. E. 1977. Coherent motions in the outer region of turbulent boundary layers. *Phys. Fluids, Suppl.*, **20**, S124–S132

Falco, R. E. 1983. New results, a review and synthesis of the mechanism of turbulence production in boundary layers and its modification. AIAA Paper 83-0377

Falco, R. E. 1991. A coherent structure model of the turbulent boundary layer and its ability to predict Reynolds number dependence. *Phil. Trans. R. Soc. Lond., A*, **336**, 103–129

Falco, R. E., Klewicki, J. C. and Kue, P. 1990. Production of turbulence in boundary layers and potential for modification of the near-wall region. In *Structure of Turbulence and Drag Reduction*, A. Gyn (ed.), Springer-Verlag, New York, 59–68

Foss, J. F. and Haw, R. C. 1990. Transverse vorticity measurements using a compact array of four sensors. ASME-FED, **97**, 71–76

Foss, J. F., Klewicki, C. L. and Disimile, P. J. 1986. Transverse vorticity measurements using and array of four hot-wire probes. NASA Contract Report 178098

Foss, J. F. and Wallace, J. M. 1989. The measurement of vorticity in transitional and fully developed turbulent flows. In *Lecture Notes in Engineering*, Vol. 45, M. Gad-el-Hak (ed.), Springer-Verlag, New York, 263–321

Gad-el-Hak, M. and Bandyopadhyay, P. R. 1994. Reynolds number effects in wall-bounded turbulent flows. *Appl. Mech. Rev.*, **47**, 307–365

Head, M. R. and Bandyopadhyay, P. R. 1981. New aspects of turbulent boundary-layer structure. *J. Fluid Mech.*, **107**, 297–338

Huffman, G. D. and Bradshaw, P. 1972. A note on von Karman's constant in low Reynolds number turbulent flows. *J. Fluid Mech.*, **53**, 45–60

Jimenez, J., Moin, P., Moser, R. and Keefe, L. 1988. Ejection mechanisms in the sublayer of a turbulent channel. *Phys. Fluids*, **31**, 1311–1313

Kastrinakis, E. G. 1976. An experimental investigation of the fluctuations of the streamwise components of the velocity and vorticity vectors in a fully developed turbulent channel flow. Doctoral dissertation, Georg-August University

Kim, J., Moin, P. and Moser, R. 1987. Turbulence statistics in fully developed channel flow at low Reynolds number. *J. Fluid Mech.*, **177**, 133–166

Klewicki, J. C. 1989. On the interactions between the inner and outer region motions in turbulent boundary layers. Ph.D. dissertation, Michigan State University, East Lansing, MI, USA

Klewicki, J. C. and Falco, R. E. 1990. On accurately measuring statistics associated with small-scale structure in turbulent boundary layers using hot-wire probes. *J. Fluid Mech*, **219**, 119–142

Klewicki, J. C., Gendrich, C. P., Foss, J. F. and Falco, R. E. 1990. On the sign of the instantaneous vorticity component in the near-wall region of turbulent boundary layers. *Phys. Fluids A*, **2**, 1497–1500

Klewicki, J. C., Falco, R. E. and Foss, J. F. 1992. Some characteristics of the vortical motions in the outer region of turbulent boundary layers. *J. Fluids Eng.*, **114**, 530–536

Klewicki, J. C., Murray, J. A. and Falco, R. E. 1994. Vortical motion contributions to stress transport in turbulent boundary layers. *Phys. Fluids*, **6**, 277–286

Kreplin, H. -P. and Eckelmann, H. 1976. Propagation of perturbations in the viscous sublayer and adjacent wall region. *J. Fluid Mech.*, **95**, 305–322

Lu, L. J. and Smith C. R. 1988. Image processing of hydrogen bubble flow visualization for quantitative evaluation of hairpin-type vortices as a flow structure of turbulent boundary layers. Report FM-14, Department of Mechanical Engineering and Mechanics, Lehigh University, Bethlehem, PA, USA

Luchik, T. S. and Tiederman, W. G. 1987. Timescale and structure of ejections and bursts in turbulent channel flows. *J. Fluid Mech.*, **174**, 529–551

Murlis, J., Tsai, H. M. and Bradshaw, P. 1982. The structure of turbulent boundary layers at low Reynolds number. *J. Fluid Mech.*, **122**, 13–56

Ong, L. 1992. Visualization of turbulent flows with simultaneous velocity and vorticity measurements. Ph.D. dissertation, University of Maryland, College Park, MD, USA

Piomelli, U., Balint, J. -L. and Wallace, J. M. 1989. On the validity of Taylor's hypothesis for wall-bounded flows. *Phys. Fluids A*, **1**, 609–611

Prandtl, L. 1925. Bericht über Untersuchungen zur ausgebildeten Turbulenz. *ZAMM*, **5**, 136–139

Purtell, L. P., Klebanoff P. S. and Buckley F. T. 1981. Turbulent boundary layer at low Reynolds number. *Phys. Fluids*, **24**, 802–811

Rajagopalan, S. and Antonia, R. A. 1993. Structure of the velocity field associated with spanwise vorticity in the wall region of a turbulent boundary layer. *Phys. Fluids A*, **5**, 2502–2510

Robinson, S. K. 1991. Coherent motions in the turbulent boundary layer. *Ann. Rev. Fluid Mech.*, **23**, 601–639

Smith, C. R., Walker, J. D. A., Haidari, A. H. and Sobrun, U. 1991. On the dynamics of near-wall turbulence. *Phil. Trans. R. Soc. Lond. A*, **336**, 131–175

Spalart, P. 1988. Direct simulation of a turbulent boundary layer up to $R_\theta = 1410$. *J. Fluid Mech.*, **187**, 61–98

Taylor, G. I. 1932. The transport of vorticity and heat through fluids in turbulent motion. *Proc. Roy. Soc.*, **A135**, 685–706

Tennekes, H. and Lumley, J. L. 1972. *A First Course in Turbulence*, 211

Van Driest, E. R. 1956. On turbulent flow near a wall. *J. Aero Sci.*, **23**, 1007–1011

Wallace, J. M. and Foss, J. F. 1995. The measurement of vorticity in turbulent flows. *Ann. Rev. Fluid Mech.*, **27**, 469–514

Wei, T. and Willmarth, W. W. 1989. Reynolds number effects on the structure of a turbulent channel flow. *J. Fluid Mech.*, **204** 57–95